Supplementary Information for
Millimeter-wave dielectric tunability driven by topological polar structure switching in $PbTiO_3/SrTiO_3$ superlattices

Sixu Wang[1,#], Jiyuan Yang[2,#], Hanbin Gao[3,#], Kazuki Okamoto[4,#], Rui Liu[5], Yunpeng Ma[1], Tao Zhou[5], Martin Holt[5], Qiang Zheng[3], Hiroshi Funakubo[4], Shi Liu[2,6,*], Jing-Feng Li[1], Qian Li[1,*]

1. State Key Laboratory of New Ceramic Materials, School of Materials Science and Engineering, Tsinghua University, Beijing, 100084, China
2. Department of Physics, School of Science and Research Center for Industries of the Future, Westlake University, Hangzhou, Zhejiang, 310030, China
3. CAS Key Laboratory of Standardization and Measurement for Nanotechnology, National Center for Nanoscience and Technology, Beijing, 100190, China
4. School of Materials Science and Engineering, Institute of Science Tokyo, Yokohama, Kanagawa 226-8501, Japan
5. Center for Nanoscale Materials, Argonne National Laboratory, Lemont, IL 60439, USA
6. Institute of Natural Sciences, Westlake Institute for Advanced Study, Hangzhou, Zhejiang, 310024, China

# These authors contribute equally to this work.
* Corresponding authors: qianli_mse@tsinghua.edu.cn (QL), liushi@westlake.edu.cn (SL)

This file includes:

Supplementary Tables 1–2
Supplementary Notes 1–3
Supplementary Figures 1–9

Supplementary Table 1 | Sample structural information of $[(PbTiO_3)_n/(SrTiO_3)_8]_m$ superlattices

n	***m***	**Total thickness**	**Out-of-plane period**	**In-plane period**	**Average lattice constant *c***
12	23	183.2 nm	8.0 nm	9.1 nm	3.960 Å
15	19	173.0 nm	9.1 nm	10.4 nm	3.969 Å
20	16	179.5 nm	11.2 nm	12.6 nm	3.977 Å
22	14	165.1 nm	11.8 nm	13.6 nm	3.979 Å

The out-of-plane periods and average *c* are derived from the XRD measurements in Supplementary Fig. 1a. The in-plane periods are derived from rocking curve scans (ω scans) at respective 2θ positions for each film. The total thicknesses are calculated from out of plane periods and designed number of period cycles *m*.

Supplementary Table 2 | Fitted values of the domain component portion and second-order $\chi^{(2)}$ susceptibility tensor

n	**State**	χ_{11}/χ_{26}	χ_{12}/χ_{26}	***q***
15	Before	0.664	1.520	62.6%
	After	0.078	1.058	29.3%
22	Before	0.481	1.222	51.6%
	After	-0.157	0.968	29.5%

Supplementary Note 1 | Extracting domain components using second-order $\chi^{(2)}$ susceptibility tensor fitting

SHG is dependent on the symmetry of the material. We can express the SHG nonlinear polarization via a second-order nonlinear coefficient tensor as:

$$\begin{pmatrix} P_x(\varphi) \\ P_y(\varphi) \\ P_z(\varphi) \end{pmatrix} = \epsilon_0 \begin{pmatrix} \chi_{11} & \chi_{12} & \chi_{13} & \chi_{14} & \chi_{15} & \chi_{16} \\ \chi_{21} & \chi_{22} & \chi_{23} & \chi_{24} & \chi_{25} & \chi_{26} \\ \chi_{31} & \chi_{32} & \chi_{33} & \chi_{34} & \chi_{35} & \chi_{36} \end{pmatrix} \begin{pmatrix} E_x^2(\varphi) \\ E_y^2(\varphi) \\ E_z^2(\varphi) \\ 2E_yE_z(\varphi) \\ 2E_zE_x(\varphi) \\ 2E_xE_y(\varphi) \end{pmatrix} \quad \text{(S1)}$$

where $E_i(\varphi)$ is the electric field of the fundamental wave, and $P_i(\varphi)$ is the polarization of the SHG wave. For specific symmetries, certain elements in this tensor are zero, so that the tensor can be simplified with fewer nonzero elements. For *m* point group symmetry in dipole wave or flux closure structures, the $\chi^{(2)}$ susceptibility tensor is as follows:

$$\chi_1 = \begin{pmatrix} \chi_{11} & \chi_{12} & \chi_{13} & 0 & \chi_{15} & 0 \\ 0 & 0 & 0 & \chi_{24} & 0 & \chi_{26} \\ \chi_{31} & \chi_{32} & \chi_{33} & 0 & \chi_{35} & 0 \end{pmatrix} \quad \text{(S2)}$$

$$\chi_2 = \begin{pmatrix} 0 & 0 & 0 & 0 & \chi_{24} & \chi_{26} \\ \chi_{12} & \chi_{11} & \chi_{13} & \chi_{15} & 0 & 0 \\ \chi_{32} & \chi_{31} & \chi_{33} & \chi_{35} & 0 & 0 \end{pmatrix} \quad \text{(S3)}$$

when the mirror plane is perpendicular to the *y*-axis or *x*-axis, respectively. For both dipole wave and flux closure structures, the mirror plane is parallel to the net polarization direction. Therefore, χ_1 and χ_2 correspond to the topological domain structures with net polarization along the *x*- and *y*-axes, noted as the T_1 and T_2 domains in the following descriptions for simplicity, which is also shown in Fig. 3d. The 2-fold-4-fold mixture in the SHG originates from the mixture of such a_1/a_2-like domains, with 2-fold and 4-fold components from domains with different net polarizations.

In the case of normal incidence, the *z* component of the electric field of incident light should be zero, and the *z* component of the nonlinear polarization does not affect the measured SHG intensity, as the light polarization should be perpendicular to the propagation direction of the light, which is the *z*-axis direction. The focusing effect of incident light is ignored for the relatively low numerical aperture of the focusing lens. Therefore, the SHG intensity measured under *x*-out and *y*-out (α = 0° or 90°, respectively) conditions as a function of the fundamental wave polarization angle φ

can be given by $I_x(\varphi) = |P_x(\varphi)|^2$ and $I_y(\varphi) = \left|P_y(\varphi)\right|^2$, noting that only P_x and P_y contribute to the intensity of light polarized in the xy plane. It follows that $E_x(\varphi) = |E|\cos\varphi$, $E_y(\varphi) = |E|\sin\varphi$, $E_z(\varphi) = 0$, where E refers to the total electric field of the input fundamental wave. According to the measurement geometry, the external electric field is applied along the y direction. According to Eqs. S1–S3, the measured SHG intensity can be expressed as:

$$I_x(\varphi) \propto q^2(\chi_{11}\cos^2\varphi + \chi_{12}\sin^2\varphi)^2 + (1-q)^2(\chi_{26}\cdot 2\cos\varphi\sin\varphi)^2 \quad \text{(S4)}$$

$$I_y(\varphi) \propto (1-q)^2(\chi_{12}\cos^2\varphi + \chi_{11}\sin^2\varphi)^2 + q^2(\chi_{26}\cdot 2\cos\varphi\sin\varphi)^2 \quad \text{(S5)}$$

where q is the portion of the T_1 domain. Only χ_{11}, χ_{12}, and χ_{26} matter in the measured SHG intensity according to Eqs. S4 and S5. The q is close to 50% before switching, which originates from the symmetry of the substrate, where the x- and y-directions are equivalent. The values of χ_{11}, χ_{12}, χ_{26} and q are shown in Supplementary Table 2, with "Before" and "After" corresponding to before and after the switching process, respectively. The different values of the ratios of χ_{11}, χ_{12} and χ_{26} before or after switching can be attributed to minor structural changes remaining after recovering from the switching, as described in the main script.

Supplementary Note 2 | Calculation of dielectric constant from MD simulation

The simulated dielectric constant of the dipole wave and flux closure shown in Fig. 4d,e are calculated from MD simulation with the same model in Fig. 2d,e. The net polarization of the model is aligned along the y-axis. The superlattice film is considered as two parts, corresponding to the domains with different net polarization directions. The first one is the part with net polarization perpendicular to the electric field (T_1), whose proportion in the superlattice decreases as the field is applied. In this process, the topological polar structure should be unaffected because of its alignment. Therefore, the dielectric constant of this part is regarded as a constant, which is derived from the model with no DC electric field and a pulsed electric field along x-axis. The second is the part with net polarization parallel to the electric field (T_2), in which the polarization evolves as the field is applied. Different calculations with both a varying DC electric field and a pulsed electric field along the y-axis were undertaken. In all the models mentioned above, the pulsed electric field is a Gaussian pulse with a full width at half maximum of ~8.4 ps. Time-resolved polarization evolution is calculated to obtain the net polarization P along the pulsed electric field direction as a function of time t. By fast Fourier transform (FFT), the magnitude of changes in net polarization P (that is, its frequency spectrum) is derived and compared with the magnitude of the excitation pulse E. Considering the relative dielectric constant $\varepsilon_r=\Delta P/(\varepsilon_0\ \Delta E)$, by dividing the above mentioned magnitudes, the dielectric constant for each domain is derived.

The two domains can be considered as capacitors in series or in parallel. In reality, the dielectric constant of the structure should be between these two values. For simplicity, we consider the sample as parallel capacitors, as the two domains should be distributed uniformly. The proportion of the T_2 domain is considered to increase linearly as the DC electric field increases and shares the same maximum proportion with the measured value derived from the 3D RSM in Fig. 3g and Supplementary Note 1 above, as the electric field applied in the model is different from that in the experiments because of the different switching fields.

Note that owing to the larger switching voltage in the model compared with the experimental results, the electric field applied on the model is larger than that in the experiments, therefore introducing greater tunability.

Supplementary Note 3 | Analyzation of domain proportions from X-ray nanobeam diffraction imaging

The contrast in Supplementary Fig. 8b,f illustrates the distribution of the T_1 and T_2 topological domains, with the bright regions corresponding to T_1 and the dark regions to T_2. These bright regions are shown in yellow zones in Supplementary Fig. 8d,h. The bright areas in Fig. 1e show the location of *a*-domains tilted towards one side, also shown in Supplementary Fig. 8c, occupying 10% of the sample area. The *a*-domains tilted towards the other side occupy a similar proportion, contributing a combined total of 20% of the sample area polarized along the *x*-axis. The T_1 domains constitute 27% of the n = 12 superlattice, adding up to close to 50% with the tilted *a*-domain, which adds up to the total area with net polarization along the *x*-axis. Overall, tilted *a*-domains in all directions occupy 40% of the total area, and the dipole wave occupies the remaining 60%, among which the T_1 and T_2 domains are distributed equally.

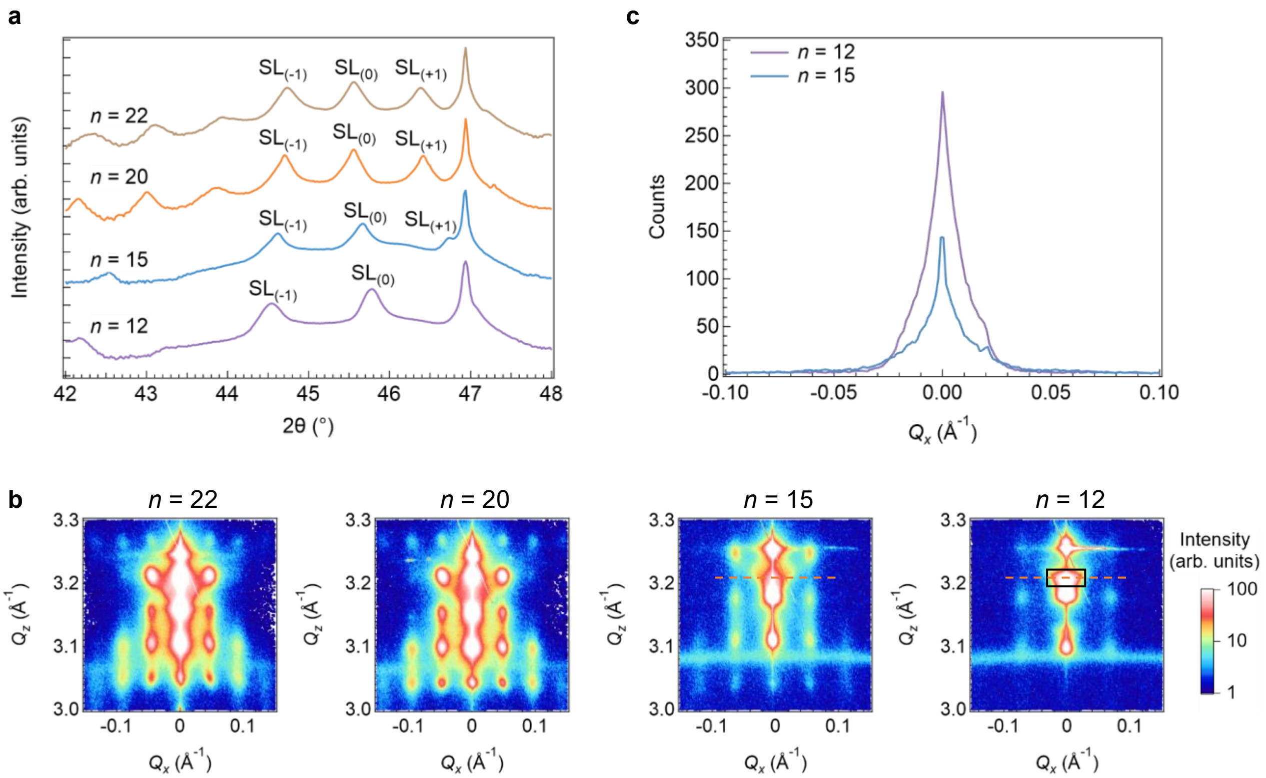

Supplementary Figure 1 | **a,** X-ray diffraction $2\theta/\omega$ scan of the superlattice samples. The 0th-order peak of the superlattice is marked in the figure. **b,** $H0L$-slice (at $Q_y = 0$ Å^{-1}) X-ray RSM around the LSAT 002 reflection for $(PbTiO_3)_n/(SrTiO_3)_8$ superlattices with n = 22, 20, 15, and 12. The square mark shows the diffraction of the tilted ferroelectric *a*-domains in the n = 12 superlattice. **c,** Line cuts along the dashed lines ($Q_z = 3.21$ Å^{-1}) for n = 15 and 12 superlattices in (b), showing in-plane ordering across the first-order superlattice peaks. The full widths at half maximum of the peaks are 0.015 Å^{-1} and 0.021 Å^{-1} for n = 15 and 12 superlattices, respectively.

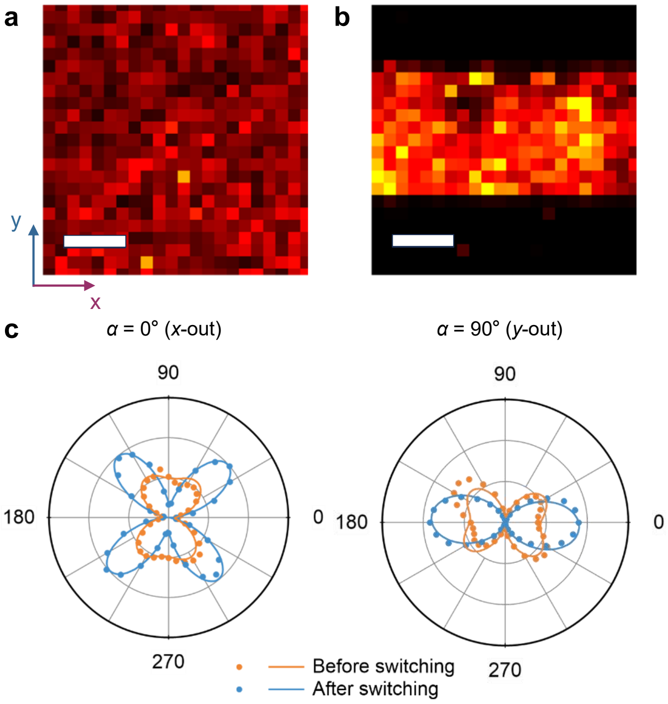

Supplementary Figure 2 | SHG measurement of $(PbTiO_3)_n/(SrTiO_3)_8$ superlattices with $n = 22$. **a,b,** SHG images outside electrode areas without switching (a) and inside electrode areas after switching (b) **c,** SHG polar plots before and after switching. The intensity after switching is divided by 10 for clarity. Scale bar = 5 µm.

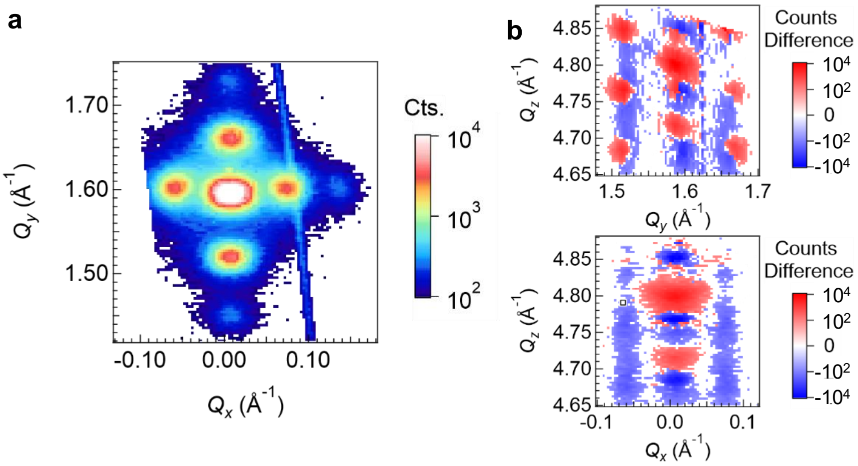

Supplementary Figure 3 | Synchrotron-based 3D RSM. **a,** The *xy* slice of the RSM at $Q_z = 4.69$ Å^{-1} in the $n = 12$ superlattice under no external electric field, displaying fourfold symmetry on the first- and second-order satellites. **b,** RSM results of *yz* and *xz* slices at "on" states at 100 V in the $n = 12$ superlattice.

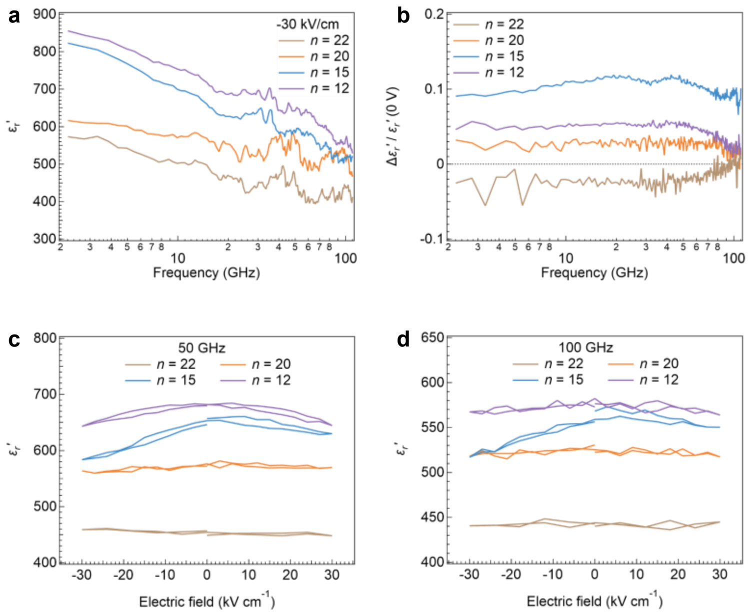

Supplementary Figure 4 | Dielectric constant modulation at different external fields in different superlattices. **a,** Dielectric spectrum of the superlattice in the in-plane direction, showing the real parts of the dielectric constant at -30 kV cm^{-1}. **b,** Dielectric tunability spectra for different superlattices, with n = 15 corresponding to Fig. 4i. **c,d,** Tuning of the real part of the dielectric constant under an electric field at 50 GHz (c) and 100 GHz (d). For n = 12 superlattices at 100 GHz, the tunability decreases but is still observable. For n = 15 superlattices at 100 GHz, the tunability is still significant.

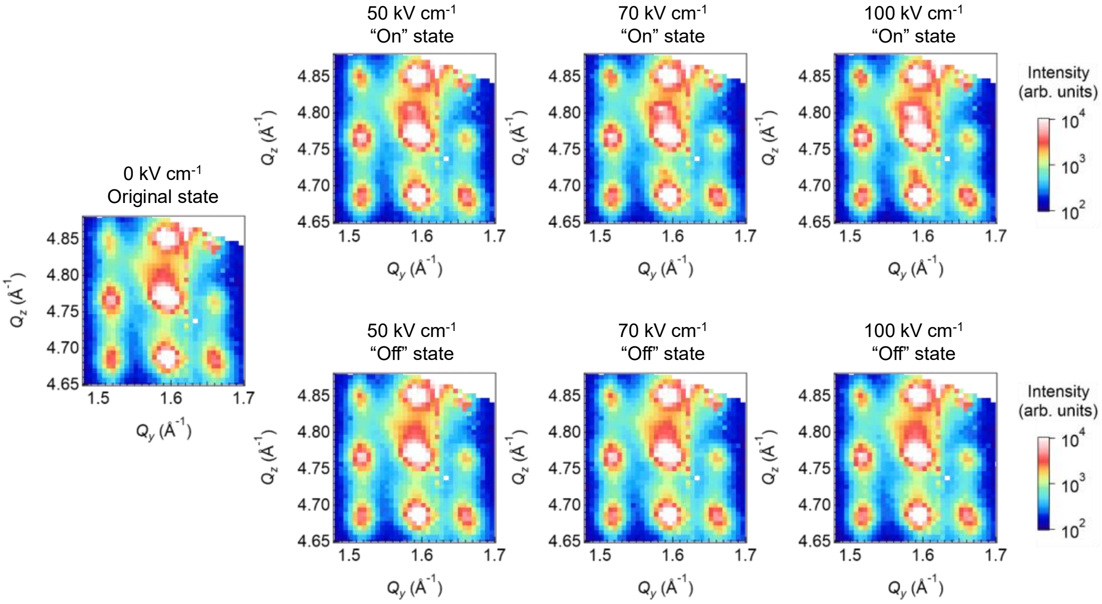

Supplementary Figure 5 | Synchrotron RSM of *yz* and *xz* slices for n =12, showing raw diffraction intensities at different voltages.

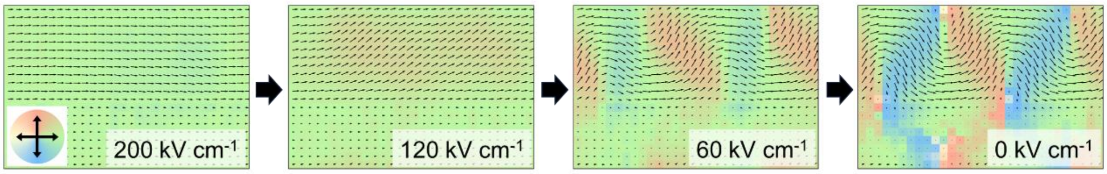

Supplementary Figure 6 | MD simulation of the polarization evolution for superlattices with $n = 12$ upon removal of the in-plane electric field after the switching process shown in Fig. 2d. The vectors show local polarizations, and the colors show their directions.

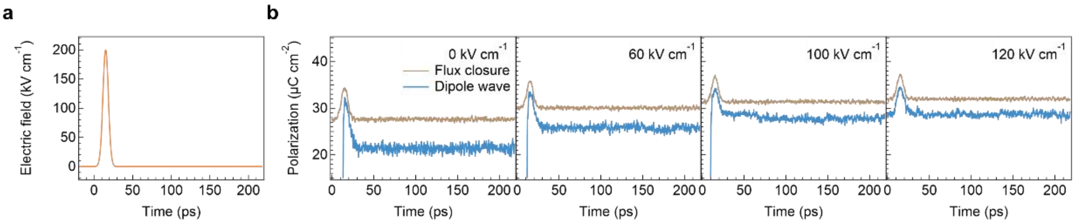

Supplementary Figure 7 | MD simulation of the dielectric permittivity. **a**, Pulsed electric field applied in the model. **b**, Net polarization P_y under different DC voltages. Smaller changes in the polarization induced by the pulse indicate a lower dielectric permittivity, which is shown in Fig. 4d.

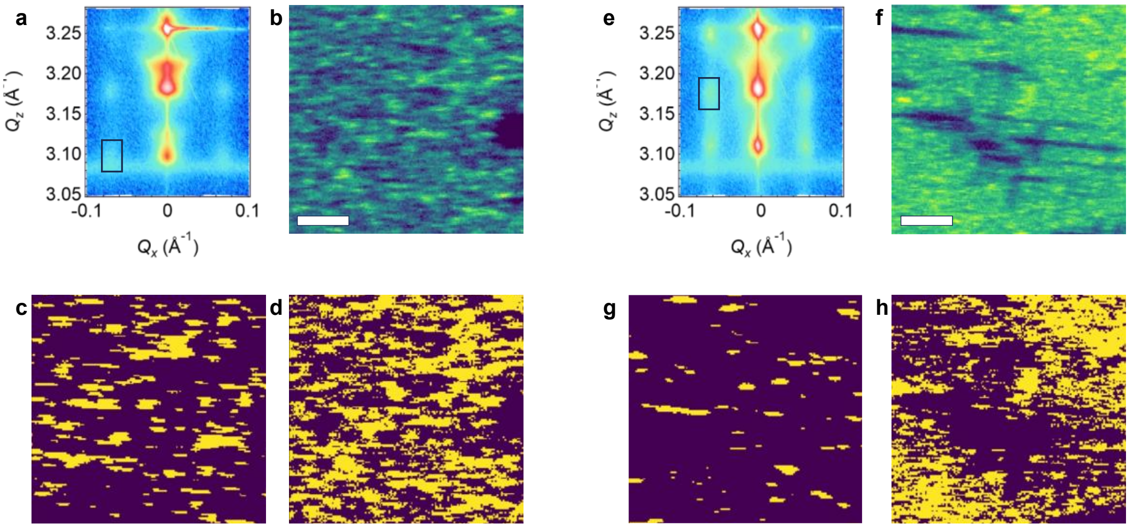

Supplementary Figure 8 | Synchrotron X-ray nanobeam diffraction mapping. **a,b,** Diffraction peaks in the $n = 12$ superlattice (a) and corresponding intensity map (b) of the marked diffraction peak in (a). **c,d,** Intensity division analyzed via the Otsu method in Python, with yellow zones showing higher intensity, from the mapping in Fig. 1e (c) and Supplementary Fig. 8b (d). **e,f,** Diffraction peaks in the *n* = 15 superlattice (e) and the corresponding intensity map (f) of the marked diffraction peak in (e). Scale bar = 2 µm. **g,h,** Intensity division analyzed via the Otsu method in Python, with yellow zones showing higher intensity, from the mapping in Fig. 1g (g) and Supplementary Fig. 8f (h).

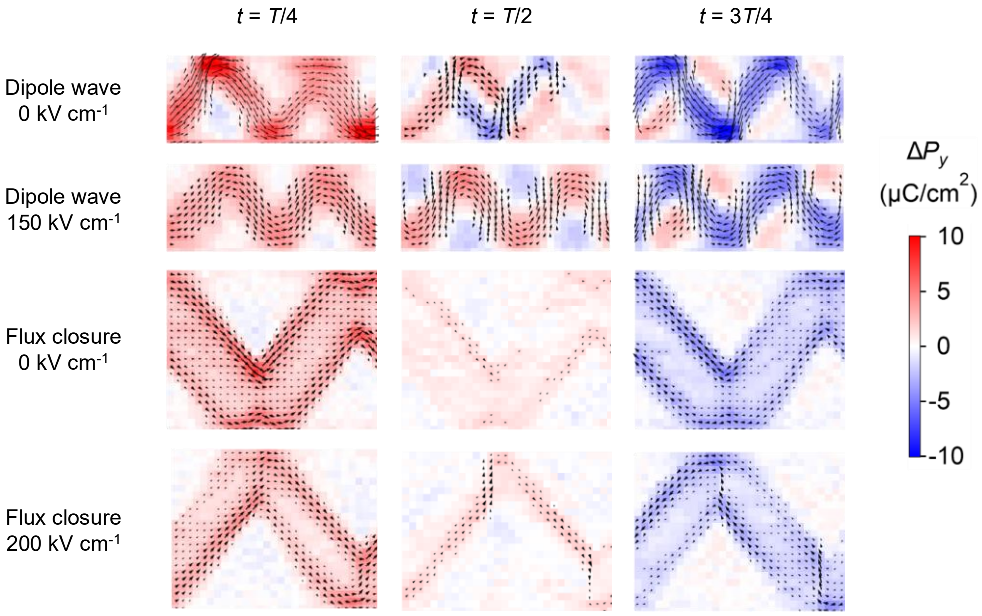

Supplementary Figure 9 | Simulated changes in polarization (ΔP) in $PbTiO_3$ layers under a sinusoidal electric field of 20 GHz at different time points in a cycle (T = 50 ps) compared to equilibrium state (t = 0).